Journal of Materials Chemistry A

A Two-electron Transfer Mechanism of Zn-doped δ-MnO_2 Cathode toward Aqueous Zn-ion Batteries with Ultrahigh Capacity

Journal:	*Journal of Materials Chemistry A*
Manuscript ID	TA-ART-12-2021-010864.R1
Article Type:	Paper
Date Submitted by the Author:	06-Feb-2022
Complete List of Authors:	Suib, Steven; University of Connecticut, U-60, Department of Chemistry Zhao, Wen; University of Connecticut Fee, Jared; University of Connecticut, Department of Chemistry Khanna, Harshul; University of Connecticut, Institute of Materials Science March, Seth ; University of Connecticut Nisly, Nathaniel; University of Connecticut Rubio, Samantha Joy B.; University of Connecticut, U-60, Department of Chemistry Cui, Can; University of Connecticut Li, Zhuo; Huazhong University of Science and Technology, Department of Materials Science and Engineering

A Two-electron Transfer Mechanism of Zn-doped δ-MnO_2 Cathode toward Aqueous Zn-ion Batteries with Ultrahigh Capacity

*Wen Zhao[1], Jared Fee[2], Harshul Khanna[1], Seth March[2], Nathaniel Nisly[2], Samantha Joy B. Rubio[2], Can Cui[1], Zhuo Li[3] and Steven L. Suib[1, 2, *]*

1. Department of Materials Science and Engineering & Institute of Materials Science, University of Connecticut, 97 N. Eagleville Rd., Storrs, Connecticut 06269-3136, United States

2. Department of Chemistry, University of Connecticut, 55 N. Eagleville Rd., Storrs, Connecticut 06269-3060, United States

3. Department of Materials Science and Engineering, Huazhong University of Science and Technology, Wuhan 430074, P. R. China.

* Email: steven.suib@uconn.edu

ABSTRACT: Neutral aqueous Zinc-ion batteries (ZIBs) have attracted considerable attention due to their safe and green features. As one typical cathode, birnessite MnO_2 (δ-MnO_2) suffers from low conductivity and structural instability, and its energy storage mechanism is still not well established yet. Herein, we developed a Zn-doped δ-MnO_2 material via a facile and effective microwave-assisted method for the cathode in aqueous ZIBs. By incorporating Zn to modify the microstructure and promote reaction kinetics, the Zn-doped δ-MnO_2 electrode demonstrates significantly enhanced electrochemical performance with an ultrahigh reversible capacity of 455 mAh g^{-1} and excellent specific energy of 628 W h kg^{-1}. In addition, the successive insertion of H^+ and Zn^{2+} and deep two-electron transfer routes are revealed systematically by *ex situ* experiments. The two-electron transfer routes (Mn^{4+}/Mn^{3+} and Mn^{3+}/Mn^{2+}) mechanism of Zn-doped δ-MnO_2

electrodes explains the exceedingly high capacity and opens new opportunities to develop high-energy aqueous ZIBs.

KEYWORDS: Manganese dioxide, Zn intercalation, microwave-assisted, aqueous Zn-ion battery, mechanism

1. Introduction

With the increasing environmental pollution caused by the long-term usage of fossil fuels, the establishment of low-carbon, green and sustainable energy systems is urgent. Rechargeable aqueous batteries have been considered as next-generation green and sustainable electrochemical energy storage technologies due to their high safety, cost-effectiveness, nontoxicity, high ionic conductivity, and easy processing in air.[1] Particularly, aqueous zinc-ion batteries (ZIBs) are emerging as one of the most compelling candidates with distinctive merits of Zn metal, such as a high theoretical capacity of 820 mAh g^{-1}, the relative low redox potential of -0.76 V vs. standard hydrogen electrode (SHE), excellent stability in water-based solutions, and nontoxicity.[2–7] As a promising cathode material for ZIBs, a variety of MnO_2-based materials have been developed given their various open-framework crystal structures and multiple oxidation states of manganese.[8–10] Different from α-, β-, R-, γ- and λ-MnO_2, δ-MnO_2 has a typical layered structure, which is more accessible to charge carriers (i.e., Zn^{2+} and H^+) and contributes to higher diffusion rates.[11–15] Unfortunately, the intrinsic conductivity of δ-MnO_2 is still unsatisfactory. Moreover, the layered δ-MnO_2 suffers from capacity loss due to the structural collapse in the process of charge/discharge.[16,17]

Defect engineering including doping has been developed as a powerful strategy to enhance the intrinsic electrochemical reactivity and structural stability of δ-MnO_2 cathodes.[14,18] Many studies

have demonstrated successful doping of heteroatoms into the bulk MnO_2 to improve the electrochemical stability and reversibility in aqueous ZIBs, including nonmetal such elements as N, transition metal ions such as V, Fe, Co, Cu, Ag, and rare earth ions such as Ce.[4,19,20] Experimental and theoretical studies have confirmed several merits of doping. First of all, doping could adjust the surface morphology of MnO_2 and extend the surface area for more electroactive sites. In addition, heteroatoms-doped MnO_2 with enriched defects facilitates the adsorption and diffusion of electrolyte ions due to the modified surface chemistry. Moreover, electron migration will be promoted by tunning the intrinsic electronic structure, which finally contributes to the outstanding electrochemical performance of MnO_2 cathodes.[21] All these benefits inspired us to develop Zn-doped MnO_2 with fine nanostructures to improve its performance in aqueous ZIBs. The intercalation of low valence cations such as Zn^{2+} can enhance the intrinsic conductivity and boost ion diffusion kinetics by introducing oxygen vacancies, which serve as shallow donors and contributes to the n-type conductivity of δ-MnO_2.[22] This is also an effective approach to stabilize the structure through the coordination of Zn^{2+} with oxygen ions on manganese polyhedra to suppress Mn dissolution.[23]

In general, most reported MnO_2-based ZIBs showed a limited capacity of less than 300 mAh g^{-1}. The conventional energy storage/release mechanism of the aqueous Zn/MnO_2 system was built on the insertion/deinsertion of charge carriers and the reversible reaction between Mn^{4+} and Mn^{3+}, which gives a theoretical capacity of 308 mAh g^{-1}. There are mainly three charge storage mechanisms, namely the reversible intercalation of Zn^{2+}, the chemical conversion reaction, and the consequent H^+ and Zn^{2+} insertion mechanism. In Boeun et al.'s study, the mechanism during the electrochemical cycling involves the reversible intercalation of zinc ions, accompanied by a reversible phase transition between tunneled (α-MnO_2) and layered MnO_2 polymorphs (Zn-

buserite).[12] Pan et al. revealed a chemical conversion reaction mechanism between MnOOH and MnO_2, and H^+ was mainly responsible for the reversible capacity of 285 mAh g^{-1} and high cycling stability.[24] In 2017, Wang's group proposed a consequent H^+ and Zn^{2+} insertion mechanism in Zn/MnO_2 battery chemistry.[25] The electrodeposited MnO_2 experienced successive H^+ and Zn^{2+} insertion with distinctly different reaction kinetics during the discharging process, which attributed to the formation of MnOOH and $ZnMn_2O_4$ phases, respectively. Increasingly, some aqueous MnO_2-based ZIBs exhibiting superior capacities higher than the theoretical value have been reported in recent years.[18,26–29] Nevertheless, to our knowledge, the expected energy storage mechanism and persuasive explanations to the large capacity higher than the theoretical value are still lacking.

In this work, the incorporation of Zn^{2+} into layered δ-MnO_2 was synthesized via a facile, effective microwave-assisted method, which possesses numerous benefits, such as rapid volumetric heating, fairly reduced reaction time, good homogeneity, morphology controllability, low cost and high yield. The as-prepared Zn-doped δ-MnO_2 was used as a cathode material in aqueous ZIBs and delivered an ultrahigh specific capacity of 455 mA g^{-1}, remarkable specific energy of 628 W h $kg^{-1,}$ and good stability with 66% retention of initial capacity after 100 cycles at a low current density of 200 mA g^{-1}. The uniformly distributed nanoflakes of Zn-doped δ-MnO_2 provide an interconnected network for ion diffusion, and its large-interspacing layered structure facilitates cation insertion/extraction. Moreover, the existence of Zn^{2+} helps maintain the framework structure stability, which is beneficial to raising performance during long-term cycling. Combining a comprehensive study of the electrochemical properties, crystal structure, composition and valence state, we confirmed a successive H^+ and Zn^{2+} insertion accompanied by two-electron transfer route mechanism. The two-electron transfer reactions between Mn^{4+} and

Mn^{2+} give an elevated theoretical capacity of 616 mAh g^{-1}, which should provide insights into high-energy aqueous MnO_2-based ZIBs.

2. Experimental section

2.1 Synthesis of Zn intercalated δ-MnO_2

The δ-MnO_2 nanoflakes with 1% Zn intercalation were prepared by a microwave-assisted hydrothermal method. In a typical synthesis, 100 mg β-cyclodextrin, 400 mg $KMnO_4$ and 3.4 mg $ZnCl_2$ were mixed and dissolved in 100 mL distilled deionized water (DDW) in a beaker under magnetic stirring. Subsequently, the solution was divided into 5 small vessels and then transferred to a microwave reactor (Monowave 450, Anton Paar). The reaction temperature was controlled at 120 ℃ with a ramp rate of 5 ℃ min^{-1} and a holding time of 15 min. The resulting precipitate was collected and washed with ethanol and DDW three times, respectively. Then, the as-prepared product was dried in an oven at 80 ℃ for 12 h. For comparison, the pristine layered δ-MnO_2 was also prepared under the same conditions but without adding $ZnCl_2$ for ion intercalation. All reagents used were of analytical grade and were supplied by Sigma-Aldrich.

2.2 Materials characterization

The crystal structure of the as-prepared samples and post-cycling electrodes was determined by X-ray diffraction spectrometry (XRD) using a Rigaku SmartLab multipurpose X-Ray diffractometer with Cu Kα radiation ($\lambda = 0.154$ nm). The morphology of the samples was characterized via scanning electron microscopy (SEM, Verios 460L SEM), transmission electron microscopy (TEM, Thermo Fisher Scientific Titan Themis Aberration Corrected Electron Microscope). The porosity and surface area were studied by Brunaure-Emmett-Teller (BET) on a Quantachrome Autosorb-1-1C automated adsorption system. Thermogravimetric analysis (TGA) was conducted on a Hi-Res TGA 2950 Thermogravimetric Analyzer to record the weight loss in

an air atmosphere from room temperature to 750 ℃ at a heating rate of 10 C/min. The surface chemistry was analyzed using X-ray photoelectron spectroscopy (XPS) on a PHI Model 590 spectrometer with an Al Kα source and all binding energies were referenced to the C 1s peak (284.8 eV). Elemental compositions of electrodes were determined by X-ray fluorescence (XRF) using a Rigaku ZSX Primus IV sequential wavelength-dispersive XRF diffractometer and Auger electron spectroscopy (AES) using an RBD instruments PHI 660 with a LaB6 filament as the electron beam source. Raman spectra were collected using a Renishaw 2000 Ramascope Micro-Raman coupled with a 514 nm Ar ion laser.

2.3 Electrochemical measurement

The electrochemical performance of the electrodes was tested with CR2032 coin cells. A coin cell was assembled with Zinc metal as the anode, aqueous 2 M $ZnSO_4$ + 0.2 M $MnSO_4$ as the electrolyte. To prepare cathodes, a slurry was made by adding 80 wt.% active materials, 10 wt.% carbon black (Super P), and 10 wt.% Polyvinylidene difluorides (PVDF) into N-Methyl-2-Pyrrolidone (NMP) solvent. The as-prepared slurry was ground for 30 min and then coated on a stainless-steel foil by using a film applicator with a thickness of 100 um. Then the foil was dried at 100 ℃ for 12 h in a vacuum oven and punched into 15-mm-diameter disks for use as the working electrode in ZIBs. The average mass loading of pristine δ-MnO_2 and Zn-doped δ-MnO_2 is 2.4 and 2.2 mg, respectively. A cathode-free ZIB was assembled with Zinc metal as the anode, aqueous 2 M $ZnSO_4$ + 0.2 M $MnSO_4$ as the electrolyte, and stainless steel as the cathode. Cyclic voltammetry (CV) was performed on batteries to study the charge storage mechanism with the voltage range 1.0-1.8 V vs. Zn^{2+}/Zn. Electrochemical impedance spectroscopy (EIS) was applied to study the resistance of batteries with an amplitude of 5 mV and a frequency range of 100 kHz to 0.01 Hz. Both CV and EIS were tested on an electrochemical workstation (Gamry Reference 600). The

galvanostatic charge/discharge performance of the batteries was analyzed on an MTI battery analyzer with the voltage range of 1.0 V to 1.8 V (vs. Zn/Zn^{2+}).

3. Results and discussion

3.1 Materials characterization

The detailed fabrication process of Zn-doped δ-MnO_2 is described in the Experimental Section and the schematic illustration is provided in Fig. S1. As shown in Fig 1a and 1d, scanning electron microscopy (SEM) images reveal that both pristine and Zn-doped MnO_2 materials adopt an interconnected nanoflake morphology. Further microstructure features of samples were investigated by transmission electron microscopy (TEM), as presented in Fig. 1b and 1e. With the moderate incorporation of foreign ions, Zn-doped MnO_2 nanoflakes display more uniform and well-established networks. The doping of Zn^{2+} into pristine MnO_2 gives rise to an effective modulation of the morphology, which is expected to be beneficial to structural stability. The high-angle annular dark-field scanning transmission electron microscopy (HAADF-STEM) data in Fig. 1c and f show that nanoflakes of both materials are crystallized with thicknesses of merely 3–5 nm. The clear lattice fringes with similar d-spacing correspond to the interplanar distance of the (003) planes of the rhombohedral δ-MnO_2 phase. HAADF-STEM elemental mapping images (Fig. 1g) confirm that K, Mn, O and Zn are homogeneously distributed in the Zn-doped MnO_2 nanoflakes.

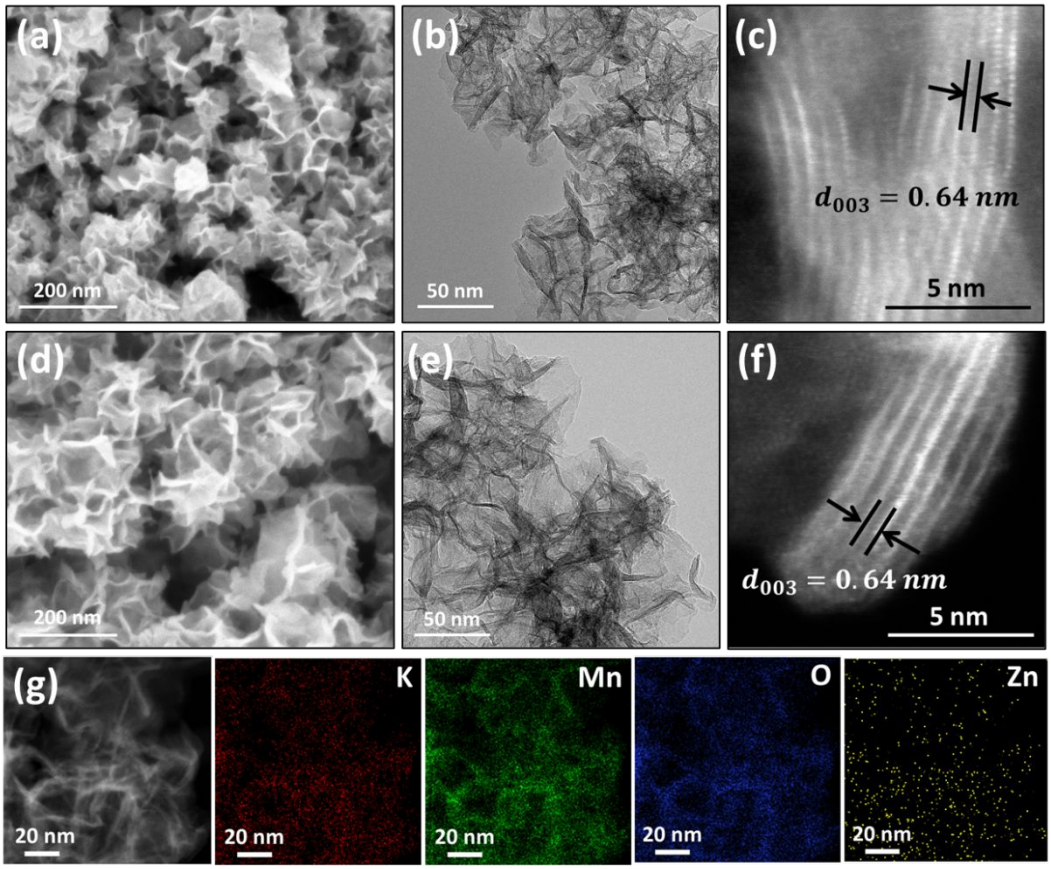

Figure 1. (a) SEM image, (b) TEM image, and (c) HAADF-STEM image of pristine MnO_2. (d) SEM image, (e) TEM image and (f) HAADF-STEM image of Zn-doped MnO_2. (g) HAADF-STEM image and elemental mapping images of Zn-doped MnO_2 nanoflakes.

The X-ray diffraction (XRD) patterns of the pristine MnO_2 and Zn-doped MnO_2 in Fig. 2a demonstrate that both materials exhibit similar crystallographic structures. There are mainly four characteristic peaks positioned at 12.3°, 24.8°, 36.8° and 65.5°, which are well indexed to (003), (006), (0012) and (110) planes of δ-MnO_2 (JCPDS 52-0556), respectively. The rhombohedral structure of $K_{0.27}MnO_2$ (a=2.849 Å, b=2.849 Å, and c=21.536 Å) is built from layers of edge-shared [MnO_6] octahedra stacked along [001] with K^+ and H_2O intercalated in the interlayer space. The peaks with broad and low intensity features are indicative of nanoscale crystallites and low crystallinity of MnO_2, which is in line with the TEM observations. There is no obvious peak shift for Zn-doped δ-MnO_2 compared with its pristine counterpart, suggesting the similar spacing

distance of the two samples. MnO_2 with layered structures requires cations and water molecules to stabilize their structural framework. There are three-stage weight losses in the TGA profiles (Fig. S2). The first stage with 12 wt.% loss before 200 °C is related to the removal of surface adsorbed water, and then the platform situating between 200-475 °C is responsible for the loss of crystallization water in MnO_2, which is typical of layered type MnO_2. The third stage above 420 °C corresponds to the partial reduction of manganese accompanied by oxygen evolution.[18,28,30] The detailed compositions and valence states of the Mn in samples were verified by X-ray photoelectron spectroscopy (XPS). The presence of the Zn element in Zn-doped MnO_2 is obvious in the full-scan XPS spectra (Fig. S3) and the high-resolution Zn 2p spectra (Fig. 2b). The shoulder peaks of Mn $2p_{1/2}$ (654.1 eV) and Mn $2p_{3/2}$ (642.4 eV) in Fig. 2c are characteristic of high-resolution Mn 2p spectrum, which has a typical spin-energy separation of 11.7 eV for MnO_2.[4,18] As shown in Fig 2d, the energy splitting of Mn 3s doublets of Zn-doped MnO_2 is 0.5 eV larger than that of pristine MnO_2, indicating the lower valence state of Mn with Zn incorporation. Specifically, additional Zn 3p peaks overlapping with Mn 3s could be observed, validating the existence of zinc ions in Zn-doped δ-MnO_2 nanoflakes. The amount of Zn doping was further examined by X-ray fluorescence (XRF) and approximately 1.4 mol % of Zn was successfully incorporated into the MnO_2 structure, as presented in Table S1. Fig. 2e and 2f show the N_2 adsorption/desorption isotherms of pristine and Zn-doped MnO_2 samples, respectively. For both samples, the remarkable hysteresis loops in the intermediate P/P_0 range illustrate a mesoporous texture, and the corresponding pore diameter distribution curves (insets) show uniform mesopores centered at around 3.8 nm. The BET surface area of Zn-doped MnO_2 (111 m^2 g^{-1}) is much larger than that of the pristine counterpart (52 m^2 g^{-1}). The mesoporous architecture and the higher specific surface area of Zn-doped MnO_2 can provide more active sites for redox reactions as well

as facilitate rapid diffusion and intercalation of electrolyte ions. Raman spectra in Fig. S4 provide fundamental vibrational modes of pristine and Zn-doped δ-MnO_2. In both materials, Raman peaks positioned at 568 and 647 cm^{-1} can be assigned to Mn-O symmetric vibrations of [MnO_6] octahedra and Mn-O stretching within the basal plane of the MnO_2 sheets.[3,19,29] The emergence of the broad peak located at 443 cm^{-1} in the Zn-doped sample is associated with Zn-O stretching, further confirming the incorporation of Zn ions.[31]

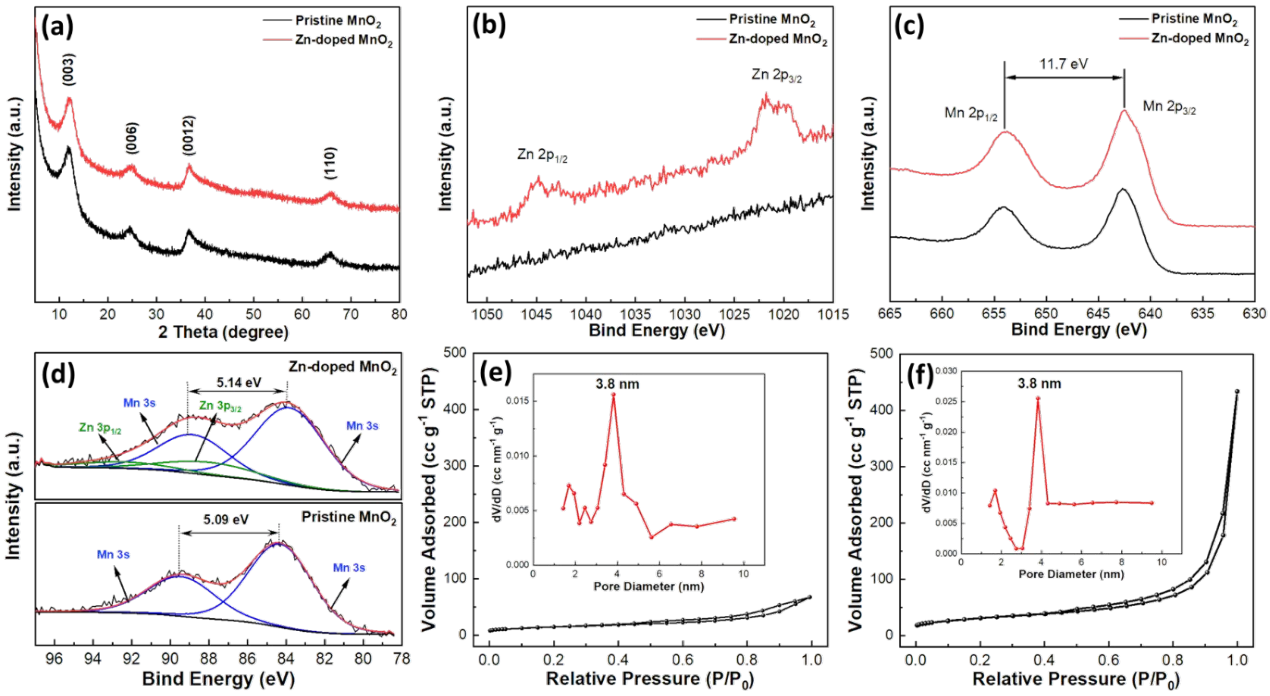

Figure 2. (a) XRD patterns, (b) high-resolution Zn 2p, (c) high-resolution Mn 2p and (d) high-resolution Mn 3s regions of XPS spectra of pristine and Zn-doped MnO_2. N_2 adsorption/desorption isotherm and the corresponding pore size distribution (inset) of (e) pristine MnO_2 and (f) Zn-doped MnO_2.

3.2 Electrochemical characterization

The electrochemical performance of pristine and Zn-doped MnO_2 was studied as the cathode in coin-type cells using Zn metal as anode and the mild aqueous solution of 2 M $ZnSO_4$ + 0.2 M $MnSO_4$ as electrolyte. The charge/discharge galvanostatic plots of both cathodes tested at 25 mA g^{-1} current density are shown in Fig. 3a and 3b. Notably, Zn-doped MnO_2 cathodes achieve an ultrahigh capacity of 455 mAh g^{-1} after a rapid increase in capacity in the first 30 cycles, much

higher than the largest capacity of the pristine MnO_2 counterpart (314 mAh g^{-1}) obtained at the 3rd cycle. In addition, an outstandingly high specific energy of 628 W h kg^{-1} was obtained for Zn-doped ZIBs. This is a very high specific capacity and specific energy, clearly surpassing most MnO_2-based and other cathode materials, such as α-(Mn_2O_3−MnO_2) heterostructures,[32] metal-organic framework $Cu_3(HHTP)_2$,[33] oxygen defect enriched $(NH_4)_2V_{10}O_{25}$ nanosheets,[34] Graphene-Wrapped MnO/C,[35] etc., as shown in Table S2. The two sloping plateaus can be mainly attributed to the redox reactions of Mn^{4+}/Mn^{3+} and Mn^{3+}/Mn^{2+}, respectively, which are in accordance with the cyclic voltammetry observations. The prolonged two plateaus of Zn-doped MnO_2 cathodes signify the enhanced H^+ insertion and Zn^{2+} insertion contributions to the discharge capacity. The enhanced electrochemical performance of Zn-doped MnO_2 can be further observed from the rate performance at different current densities from 25 to 500 mA g^{-1} in Fig. 3c. Their capacities gradually decrease with the higher current density due to the limitation of reaction kinetics. Zn-doped MnO_2 electrodes delivered considerably higher capacity than that of pristine MnO_2 electrodes at each rate. For Zn-doped MnO_2 ZIBs, a maximum discharge capacity of ~450 mAh g^{-1} was achieved at 25 mA g^{-1} and retained a capacity of 110 mAh g^{-1} at 500 mA g^{-1}, while the pristine MnO_2 ZIBs deliver a capacity of ~ 310 mAh g^{-1} at 25 mA g^{-1} and a capacity of 48 mAh g^{-1} at 500 mA g^{-1}. The specific capacity of Zn-doped MnO_2 ZIBs could return to the initial level when the current density is back to a low current rate of 25 mA g^{-1}, confirming the high reactivity and excellent rate capability of Zn-doped cathodes. The superior rate performance of Zn-doped cathodes can be attributed to the well-established and interconnected MnO_2 nanoflakes, which provide a mesoporous nanotexture for ion transportation and a higher specific surface area for more active sites. Simultaneously, the favorable layered crystal structure of MnO_2 and the incorporation of Zn ions into the crystal structure benefit the faster diffusion of electrolyte ions

inside the electrodes. The long-term cycling stability was evaluated by galvanostatic charge/discharge tests. Cycling at low current rates can destroy the structure of electrode materials, resulting in fast capacity loss. Therefore, a critical appraisal of electrochemical performance cycling at low current densities (< 0.5 A g^{-1}) is extremely ensured and sufficient electrochemical redox reactions during the deep cycling process are warranted to evaluate the structural stability of the cathode materials.[36] Excellent cycling performance is achieved for the Zn-doped MnO_2 ZIBs at a low current rate of 200 mA g^{-1}. As described in Fig. 3d, an increment of capacity in the beginning cycles was observed, which was attributed to the gradual activation process of electrodes and is very common for Zn/MnO_2 batteries in $ZnSO_4$ electrolyte with the addition of $MnSO_4$. The reversible discharge capacity of Zn-doped MnO_2 ZIBs retained 140 mAh g^{-1} after 100 cycles, much higher than the pristine MnO_2 counterpart with a capacity retention of 81 mAh g^{-1}. The cycling performance at a higher current density (500 mA g^{-1}) is also provided in Fig. S5. After 500 cycles, the Zn-doped MnO_2 ZIBs could maintain a high capacity retention of 80%, illustrating good stability. Combining the ultrahigh specific capacity, remarkable specific energy, superior rate performance, long cycle life, and environmentally friendly nature, Zn-doped MnO_2 is a promising cathode material in ZIBs.

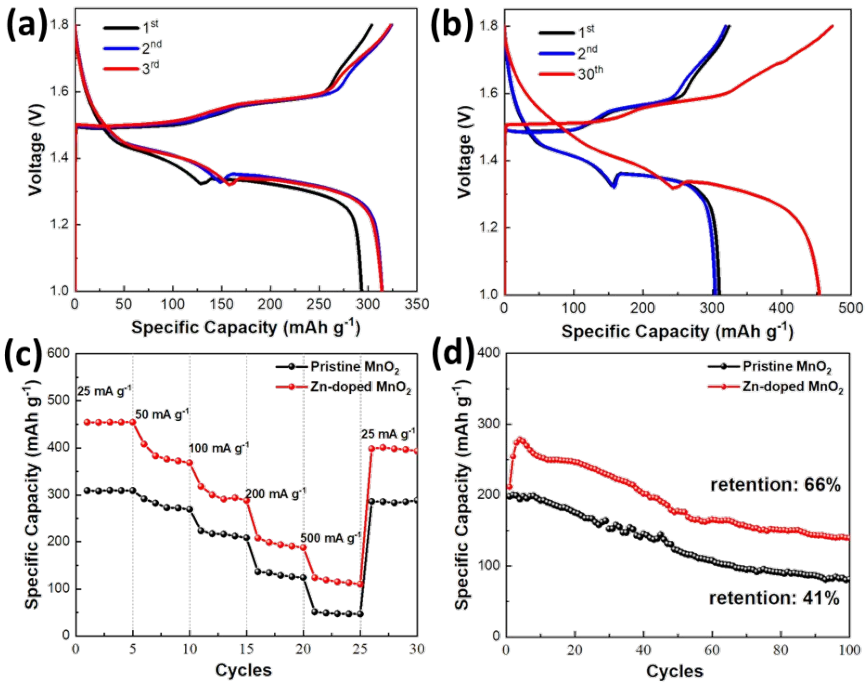

Figure 3. Discharge-charge profiles of (a) pristine MnO_2 and (b) Zn-doped MnO_2 ZIBs at a current density of 25 mA g^{-1}. (c) Rate performance of pristine and Zn-doped MnO_2 ZIBs. (d) Cycling performance of pristine and Zn-doped MnO_2 ZIBs at a current density of 200 mA g^{-1}.

3.3 Charge storage mechanism

The Zn-doped MnO_2 battery can provide an ultrahigh specific discharge capacity of 455 mAh g^{-1} at a low current density of 25 mAh g^{-1}, which is much higher than the theoretical capacity of MnO_2 (308 mAh g^{-1}) with the one-electron transfer mechanism between Mn^{4+} and Mn^{3+}. To provide further insights into the ion transport and redox reactions behind the experimental performance, the electrochemical kinetics process of Zn/MnO_2 batteries was analyzed via CV and Electrochemical Impedance Spectroscopy (EIS) experiments. Fig.4a presents the cyclic voltammetry (CV) curves of Zn-doped MnO_2 batteries at a scan rate of 0.1 mV s^{-1} after activation. In the first cycle, there are significant reduction peaks at 1.34 V (peak 4) and 1.22 V (peak 5), as well as a small peak at 1.08 V (peak 6). Two overlapped oxidation peaks are situated at 1.63 V (peak 2) and 1.66 V(peak 3), while the intensity of the peak at 1.56 V (peak 1) is relatively low. In following cycles, the current of the reduction peaks 4 and 5 becomes higher, while that of peak

6 declines. Simultaneously, the current of peaks 1, 2 and 3 increases gradually and the separation between peak 2 and peak 3 expands. Combined with CV profiles and *ex situ* XRD results of Zn-doped MnO_2 ZIBs, peaks 3 and 4 can be attributed to the redox reactions between Mn^{4+}/Mn^{3+}. Peaks 2 and 5 belong to the insertion/extraction of Zn^{2+} between MnOOH and ZSH, while peak 1 and peak 6 are related to the insertion/extraction of Zn^{2+} between $Zn_2Mn_4O_8$ and ZSH. The CV curves of Zn-doped MnO_2 ZIBs at various scan rates (Fig. S6) show that all peaks become broader with the increasing scan rates, and in stark contrast, peaks 3 and 4 start to dominate at high scan rates, as a result of better reaction kinetics of Mn^{4+}/Mn^{3+} redox reactions. Fig. 4b displays the electrochemical impedance spectroscopy (EIS) results of batteries at the open-circuit voltage (OCV) based on the pristine MnO_2 and Zn-doped MnO_2 cathodes. The Nyquist plots were fitted with the equivalent circuit shown in the inset and the fitted results are presented in Table S3. The semicircle in the high-medium frequency region reflects the electron transfer resistance (R_{ct}) at the electrode/electrolyte interface. Evidently, a much smaller R_{ct} (132 Ω) was obtained for the Zn-doped MnO_2 cell, as compared to the pristine MnO_2 cell ($R_{ct} = 407\ \Omega$), confirming an enhanced electron-transfer kinetics. Moreover, the sloping line in the low frequency region is associated with the Warburg diffusion (Z_w) of ions in the porous electrode. The ionic diffusion coefficient (D_{ion}) in the bulk phase is an important parameter for studying the kinetics of ZIBs. The line slope of the Zn-doped battery is much steeper than that of the pristine MnO_2 battery, implying a faster ion diffusion rate within Zn-doped cathodes. The lower R_{ct} and higher diffusion rate jointly render better reaction kinetics for high-rate performance of Zn-doped MnO_2 cathodes. EIS measurements were also performed on both batteries when discharged to 1.31 V vs. Zn^{2+}/Zn, which is at the middle of the second plateau. As mentioned above, the reactions at 1.31 V involve the insertion of

Zn^{2+}. Thus, the ionic diffusion coefficient of Zn^{2+} can be calculated using the following formula:[28,37,38]

$$D_{ion} = \frac{R^2T^2}{2n^4F^4A^2C_{ion}^2\sigma^2} \quad (1)$$

where R is the ideal gas constant, T is the thermodynamic temperature (298.15 K), n is the charge transfer number, F is the Faraday constant, A is the area of the electrode surface (1.76 cm^2), and C_{ion} reflects the ionic concentrations. σ is the Warburg coefficient, which can be obtained by calculating the slope of Z' against $\omega^{-1/2}$. The ionic diffusion coefficient of Zn^{2+} ($(D_{Zn^{2+}})$ in Zn-doped MnO_2 cathodes is calculated to be about 3.61×10^{-12} cm^2 s^{-1}, which is much higher than that in pristine MnO_2 cathodes (6.25×10^{-13} cm^2 s^{-1}). The enhanced Zn^{2+} ion diffusion is attributed to the Zn incorporation with favorable interconnected nanoflake morphology and optimized intrinsic electronic structure, which improves the ion migration and ameliorates the electronic conductivity of the Zn-doped MnO_2 active material.

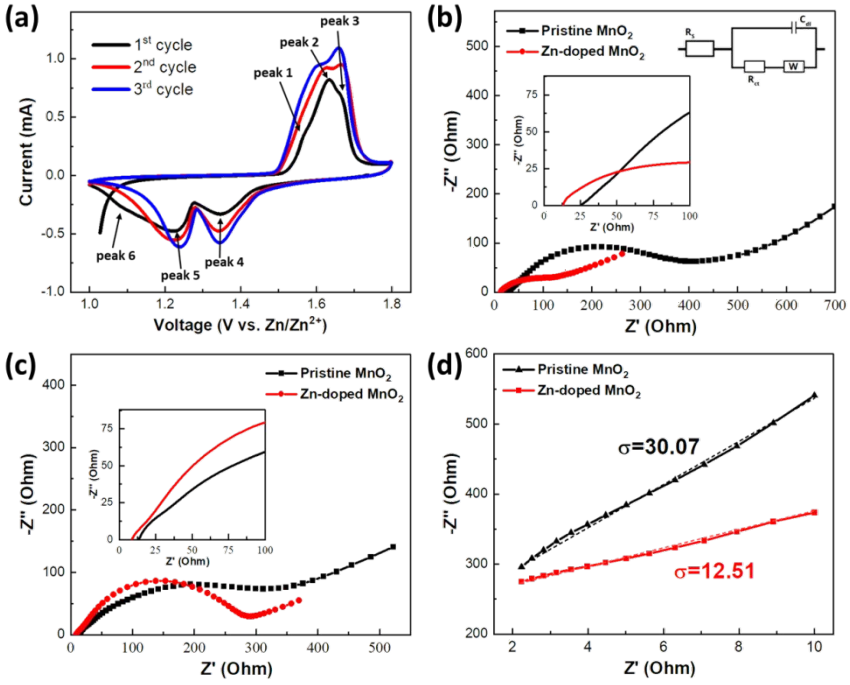

Figure 4. (a) CV curves of Zn-doped MnO_2 ZIBs at 0.1 mV s^{-1} after activation. (b) Nyquist plots of pristine MnO_2 and Zn-doped MnO_2 ZIBs at the open-circuit voltage and the corresponding equivalent circuit model (inset). (c) Nyquist plots of pristine MnO_2 and Zn-doped MnO_2 ZIBs at 1.31 V vs. Zn^{2+}/Zn.

To investigate phase evolution and the energy storage mechanism of Zn-doped MnO_2 cathodes, the electrode was discharged and charged to different states, at which the crystal structure, composition and valence state of Mn were systematically characterized. *Ex situ* XRD analysis was performed on cathodes at different voltages. The overall evolution and the corresponding voltage-time curve notated with V1 to V9 are presented in Fig. 5a and the schematic discharge process is presented in Fig. 5b. The detailed XRD patterns at specific positions are shown in Fig. 5c-d, in which the unmarked peaks located at 74.7°, 43.6°, and 44.0° originate from the stainless steel substrate and super P (as shown in Fig. S11) and are used as the references to align diffraction peaks. When the battery was discharged from V1 (1.80 V) to V2 (1.44 V), the capacity was mainly attributed to the insertion of H^+ into the layer spacing of birnessite MnO_2. There is no significant phase change or peak shift due to the small size of H^+ ions and the large distance between [MnO_6] octahedra layers. The reaction (2) took place between V1 and V2. Subsequently, with the battery further discharged to the turning point V3 (1.31 V), Zn^{2+} insertion started to dominate the reaction in cathodes. $Zn_2Mn_4O_8$ (JCPDS 09-0459) formed via a one-electrode transfer reaction (eq. (3)). Meanwhile, the consumption of H^+ in reaction (2) generated an accumulation of OH^- ions with an increased pH value in the vicinity of the electrode surface, resulting in the gradual precipitation of $Mn(OH)_2$. With continued discharging from the turning point V3, a new phase with evident characteristic peaks appeared and grew in the second discharge plateau, which can be assigned to $Zn_4SO_4(OH)_6$ (ZSH, JCPDS 09-0204). With Zn^{2+} insertion, the MnOOH phase transformed into ZSH and released a lot of H^+, leading to the dissolution of $Mn(OH)_2$ at V4 (1.28 V), simply expressed as eq. (4). After further discharging to V5 (1.00 V), the intensified diffraction peaks of ZSH and the emergence of the $Mn(OH)_2$ phase indicate that the $Zn_2Mn_4O_8$ phase formed in the first plateau was reduced to $Mn(OH)_2$ and ZSH phases with continuous Zn^{2+} insertion via reaction

(5). Electron energy-loss spectroscopy (EELS) profiles of manganese $L_{2,3}$ edges in Fig. S7 also confirm the existence of Mn^{2+} in Zn-doped MnO_2 cathodes at V5. Upon charging, the evolution of phases is the reverse process of the discharge reactions. As shown in Fig. 5d, Zn^{2+} ions were extracted from ZSH from V5 to V7 (1.50 V), while $Mn(OH)_2$ was oxidized and transformed to $Zn_2Mn_4O_8$. With continuous Zn^{2+} extraction and consumption of H^+, the ZSH phase disappeared gradually, accompanied by the formation of $Mn(OH)_2$ at V8 (1.61 V). Then Zn^{2+} and H^+ ions were released from $Zn_2Mn_4O_8$ and MnOOH via Mn^{3+}/Mn^{4+} redox reactions and dissolved $Mn(OH)_2$ at V9 (1.80 V). The active material recovered to the original phase at the final charged state, suggesting the high reversibility of Zn-doped δ-MnO_2 cathodes. To verify the capacity contribution of Mn^{2+} in the electrolyte due to MnO_2 dissolution/deposition, we analyzed cathode-free ZIBs using 2 M $ZnSO_4$ + 0.2 $MnSO_4$ as the electrolyte and stainless steel as the cathode.[39,40] Fig. S9 shows the charge/discharge plots tested at a low current of 0.06 mA, which reveals that the contribution of Mn^{2+} in the electrolyte is very limited. The pre-added Mn^{2+} provides a chemical adsorption function towards H^+ and OH^- during both H^+ and Zn^{2+} insertion/deinsertion procedures, which acts as a buffer toward pH changes and deepens the degree of redox reactions. The content of Zn and Mn elements in cathodes was measured via Auger electron spectroscopy (as shown in Fig. S12). The relative atomic concentration of Zn did not change significantly from V1 to V2 and the dramatic increase of Zn confirms the insertion of Zn^{2+} from V2 to V4. At V5, the relative amount of Mn increased because of the formation of $Mn(OH)_2$ in the alkaline environment on the surface of electrodes. *Ex situ* XPS was also conducted to analyze the detailed composition and the valence change of Mn at different states of the charge/discharge processes. In general, the intensity of Zn signals, (e.g., Zn 2s, Zn 3s, Zn 2p and Zn LMM peaks) were detected to increase with discharging (V1 to V5) and gradually decline upon charging (V5 to V9), as shown in the full-scan

XPS spectra of Zn-doped MnO_2 cathodes at different states (Fig. S13b). Specifically, the Mn 3s core-level spectra in Fig. 5e showed an energy separation of 5.2, 5.5, and 5.7 eV at V1, V3 and V5 states, respectively. The distinct increase of peak splitting indicates the reduced oxidation state of Mn during the discharge process. In the same region, the increased percent of deconvoluted high-resolution Zn 3p contribution confirmed the Zn insertion during discharging. Conversely, in the charge process (V5 to V9), the reduced energy splitting between Mn 3s peaks shows the oxidation of Mn; the reduced intensity of Zn 3p verifies the extraction of Zn^{2+} from the host materials. As shown in Fig. 5f, the O1s high-resolution spectra can be split into three contributions, which can be assigned to tetravalent Mn-O-Mn (530.3 eV), hydrated trivalent Mn-O-H (531.7 eV), and H-O-H (532.7 eV) bonds. The major peak of low valence Mn at 531.7 eV significantly increased after the electrode was discharged and then dropped when charged, indicating the reduction of Mn in cathodes, which is in accordance with the core-level Mn 3s spectra. The deconvoluted peaks of both Mn3s and O1s at V9 are consistent with the original state at V1, indicating the complete recovery after each cycle.

$$MnO_2(s) + H_2O(l) + e^- \leftrightarrow MnOOH(s) + OH^-(aq) \quad (2)$$

$$4MnO_2(s) + 2Zn^{2+}(aq) + 4e^- \leftrightarrow Zn_2Mn_4O_8(s) \quad (3)$$

$$MnOOH(s) + 4Zn^{2+}(aq) + SO_4^{2-} + 4H_2O(l) + e^- \leftrightarrow Zn_4SO_4(OH)_6(s) + Mn^{2+}(aq) + 3H^+(aq) \quad (4)$$

$$Zn_2Mn_4O_8(s) + 2Zn^{2+}(aq) + SO_4^{2-}(aq) + 8H_2O(l) + 4e^- \leftrightarrow Zn_4SO_4(OH)_6(s) + 4Mn(OH)_2(s) + 2OH^-(aq) \quad (5)$$

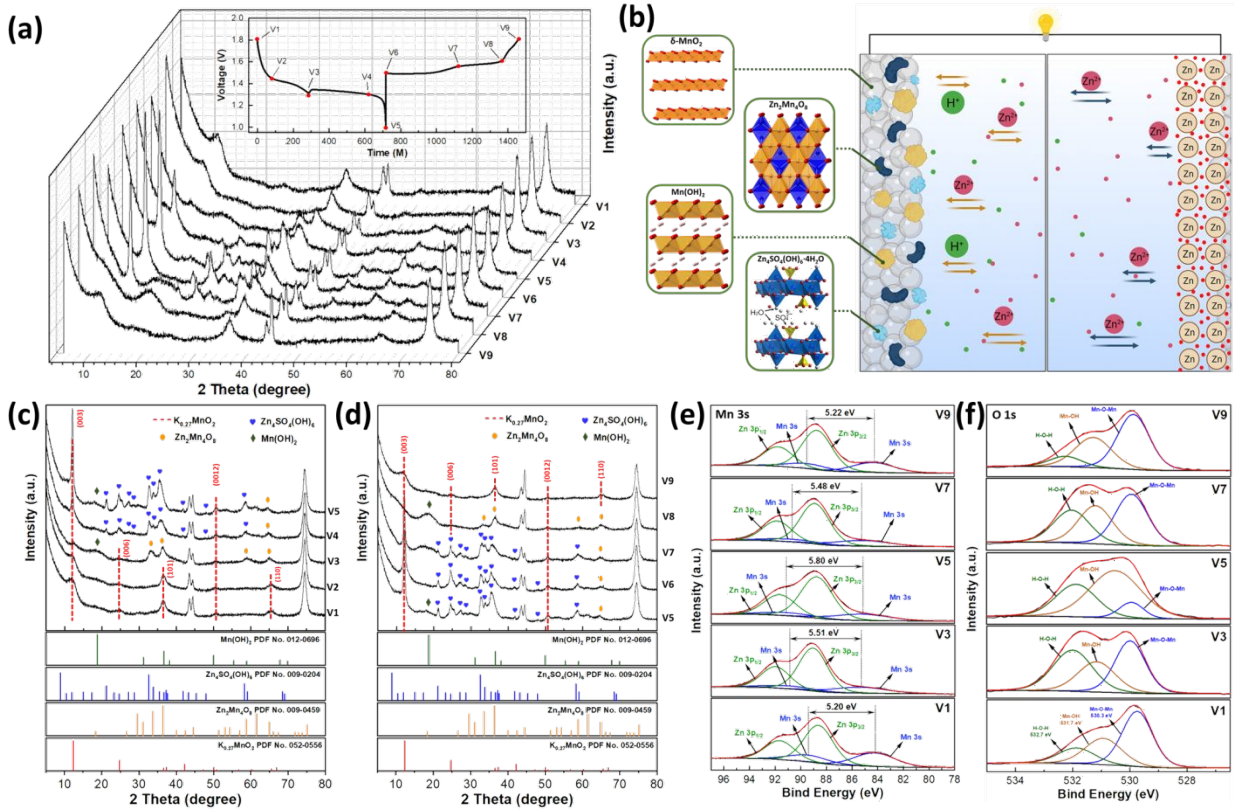

Figure 5. (a) Overall evolution of *ex situ* XRD patterns of Zn-doped MnO_2 cathodes and the corresponding voltage-time curve (inset). (b) Schematic illustration of the discharge/charge process in ZIBs. *Ex situ* XRD patterns of Zn-doped MnO_2 cathodes during (c) the discharge process (V1 to V5) and (d) the charge process (V5 to V9). *Ex situ* high-resolution Mn3s XPS spectra during (e) the discharge process (V1 to V5) and (f) the charge process (V5 to V9).

The above phenomenon indicates that MnOOH and $Zn_2Mn_4O_8$ serve as intermediate phases and will transform into ZSH and Mn^{2+} as the discharge proceeds. Eventually, two-electron transfer routes can be achieved. The similar XRD patterns of pristine MnO_2 cathodes at different voltages in Fig. S14 suggest both materials adopt two-electron transfer routes to achieve capacities higher than 308 mAh g^{-1}. As shown in Fig. S15, Zn-doped MnO_2 ZIBs exhibited an activation process as both Mn^{4+}/Mn^{3+} and Mn^{3+}/Mn^{2+} redox reactions intensified from the 1st to the 30th cycles, while the capacity contribution of reactions between Mn^{3+}/Mn^{2+} decayed with cycling in pristine MnO_2 ZIBs. The incorporation of Zn into the δ-MnO_2 crystal structure can facilitate Zn^{2+} insertion and promotes two-electron transfer routes. The superior reaction kinetics of Zn-doped MnO_2 cathodes

may be due to the enhanced electronic conductivity and greatly improved specific surface area, which could provide shorter ion diffusion lengths and increase active sites for Zn^{2+} intercalation. Fig. S16 presents the XRD patterns of the pristine and Zn-doped MnO_2 cathodes at the 30th and 100th discharged states. In pristine MnO_2 cathodes, the phase was completely transferred to $Zn_2Mn_4O_8$ after 30 cycles of charge/discharge procedures. Remarkably, typical peaks from δ-MnO_2 can still be observed in Zn-doped MnO_2 cathodes after 100 cycles. The Zn insertion/deinsertion reactions are more reversible in Zn-doped MnO_2 cathodes, which explains the higher capacity retention during the cycling stability test.

4. Conclusions

In summary, we developed a high-performance aqueous ZIB based on Zn-doped δ-MnO_2 cathodes. Through a facile and effective microwave-assisted method, the interconnected MnO_2 nanoflakes with Zn preintercalation exhibit a high specific surface area and unique mesoporous nanotexture, which provides sufficient active sites and facilitates the transportation of electrolyte ions. Additionally, the large-interspacing layered structure of birnessite MnO_2 can enhance cation insertion/extraction. The incorporation of Zn ions helps improve the intrinsic electronic conductivity of δ-MnO_2 and maintains the structural stability of the framework. This incorporation also endows the Zn-doped MnO_2 cathodes with faster charge-transfer kinetics and deeper redox reactions than the pristine MnO_2 cathodes. Benefiting from the morphological and structural merits, the as-prepared cathodes delivered an ultrahigh reversible capacity of 455 mAh g^{-1}, remarkable specific energy of 628 W h kg^{-1} and outstanding cycling stability with great capacity enhancement over 100 cycles. The energy storage mechanism is demonstrated by a consecutive insertion of H^+ and Zn^{2+} accompanied by the two-electron transfer routes between Mn^{4+}/Mn^{2+}, which is different from the majority of previously proposed one-electron transfer pathways with a theoretical

capacity of 308 mAh g^{-1}. This work throws light on the reaction mechanism of MnO_2-based cathodes in ZIBs and also provides insight into the development of next-generation high-energy aqueous energy storage devices.

Conflicts of interest

The authors declare no competing financial interest.

Acknowledgments

We acknowledge the US Department of Energy, Office of Basic Energy Sciences, Division of Chemical, Biological and Geological Sciences under grant DE-FG02-86ER13622 for support of this research.

References

1 Y. Shi, Y. Chen, L. Shi, K. Wang, B. Wang, L. Li, Y. Ma, Y. Li, Z. Sun, W. Ali and S. Ding, *Small*, 2020, **16**, 1–28.

2 F. Wan, L. Zhang, X. Dai, X. Wang, Z. Niu and J. Chen, *Nat. Commun.*, 2018, **9**, 1–11.

3 Y. Jiang, D. Ba, Y. Li and J. Liu, *Adv. Sci.*, 2020, DOI:10.1002/advs.201902795.

4 J. Wang, X. Sun, H. Zhao, L. Xu, J. Xia, M. Luo, Y. Yang and Y. Du, *J. Phys. Chem. C*, 2019, **123**, 22735–22741.

5 M. Ye, J. Shen, X. Zhu, Z. Cao, W. Wang, H. Li, J. Dong, S. Gao, D. Xu and L. Li, *ACS Nano*, 2021, **15**, 2971–2983.

6 H. Li, C. Han, Y. Huang, Y. Huang, M. Zhu, Z. Pei, Q. Xue, Z. Wang, Z. Liu, Z. Tang, Y. Wang, F. Kang, B. Li and C. Zhi, *Energy Environ. Sci.*, 2018, **11**, 941–951.

7 C. Li, X. Xie, H. Liu, P. Wang, C. Deng, B. Lu, J. Zhou and S. Liang, *Natl. Sci. Rev.*, 2021,

DOI:10.1093/nsr/nwab177.

8 J. Wang, J. G. Wang, H. Liu, Z. You, Z. Li, F. Kang and B. Wei, *Adv. Funct. Mater.*, 2021, DOI:10.1002/adfm.202007397.

9 J. Wu, X. Chi, Y. Liu, J. Yang and Y. Liu, *J. Electroanal. Chem.*, 2020, **871**, 114242.

10 A. Huang, W. Zhou, A. Wang, M. Chen, Q. Tian and J. Chen, *J. Energy Chem.*, 2021, **54**, 475–481.

11 M. H. Alfaruqi, J. Gim, S. Kim, J. Song, D. T. Pham, J. Jo, Z. Xiu, V. Mathew and J. Kim, *Electrochem. commun.*, 2015, **60**, 121–125.

12 B. Lee, H. R. Lee, H. Kim, K. Y. Chung, B. W. Cho and S. H. Oh, *Chem. Commun.*, 2015, **51**, 9265–9268.

13 S. Khamsanga, R. Pornprasertsuk, T. Yonezawa, A. A. Mohamad and S. Kheawhom, *Sci. Rep.*, 2019, **9**, 1–9.

14 L. Liu, Y. Wu, L. Huang, K. Liu, B. Duployer, P. Rozier, P. Taberna and P. Simon, *Adv. Energy Mater.*, 2021, **11**, 2101287.

15 D. S. Liu, Y. Mai, S. Chen, S. Liu, E. H. Ang, M. Ye, Y. Yang, Y. Zhang, H. Geng and C. C. Li, *Electrochim. Acta*, 2021, **370**, 137740.

16 M. X. Lin, F. Shao, S. Weng, S. Xiong, S. Liu, S. Jiang, Y. Xu, Y. Jiao and J. Chen, *Electrochim. Acta*, 2021, **378**, 138147.

17 R. D. Corpuz, L. M. De Juan-Corpuz, M. T. Nguyen, T. Yonezawa, H. L. Wu, A. Somwangthanaroj and S. Kheawhom, *Int. J. Mol. Sci.*, 2020, **21**, 1–12.

18 J. Wang, J. G. Wang, H. Liu, C. Wei and F. Kang, *J. Mater. Chem. A*, 2019, **7**, 13727–13735.

19 Y. Zhang, S. Deng, M. Luo, G. Pan, Y. Zeng, X. Lu, C. Ai, Q. Liu, Q. Xiong, X. Wang, X. Xia and J. Tu, *Small*, 2019, **15**, 1905452.

20 F. Kataoka, T. Ishida, K. Nagita, V. Kumbhar, K. Yamabuki, and M. Nakayama, *ACS Appl. Energy Mater.*, 2020, **3**, 4720-4726.

21 J. Wang, J. G. Wang, X. Qin, Y. Wang, Z. You, H. Liu and M. Shao, *ACS Appl. Mater. Interfaces*, 2020, **12**, 34949–34958.

22 G. Fang, C. Zhu, M. Chen, J. Zhou, B. Tang, X. Cao, X. Zheng, A. Pan and S. Liang, *Adv. Funct. Mater.*, 2019, **29**, 1–9.

23 G. Liu, H. Huang, R. Bi, X. Xiao, T. Ma and L. Zhang, *J. Mater. Chem. A*, 2019, **7**, 20806–20812.

24 H. Pan, Y. Shao, P. Yan, Y. Cheng, K. S. Han, Z. Nie, C. Wang, J. Yang, X. Li, P. Bhattacharya, K. T. Mueller and J. Liu, *Nat. Energy*, 2016, **1**, 1–7.

25 W. Sun, F. Wang, S. Hou, C. Yang, X. Fan, Z. Ma, T. Gao, F. Han, R. Hu, M. Zhu and C. Wang, *J. Am. Chem. Soc.*, 2017, **139**, 9775–9778.

26 X. Gao, H. Wu, W. Li, Y. Tian, Y. Zhang, H. Wu, L. Yang, G. Zou, H. Hou and X. Ji, *Small*, 2020, **16**, 1–10.

27 B. Wu, G. Zhang, M. Yan, T. Xiong, P. He, L. He, X. Xu and L. Mai, *Small*, 2018,

DOI:10.1002/smll.201703850.

28 G. Li, Z. Huang, J. Chen, F. Yao, J. Liu, O. L. Li, S. Sun and Z. Shi, *J. Mater. Chem. A*, 2020, **8**, 1975–1985.

29 H. Peng, H. Fan, C. Wang, J. Sui, C. Yang and Y. Tian, *RSC Adv.*, 2020, **10**, 17702–17712.

30 M. H. Alfaruqi, S. Islam, D. Y. Putro, V. Mathew, S. Kim, J. Jo, S. Kim, Y. K. Sun, K. Kim and J. Kim, *Electrochim. Acta*, 2018, **276**, 1–11.

31 Y. Song, S. Zhang, C. Zhang, Y. Yang and K. Lv, *Crystals*, 2019, DOI:10.3390/cryst9080395.

32 J. Long, F. Yang, J. Cuan, J. Wu, Z. Yang, H. Jiang, R. Song, W. Song, J. Mao and Z. Guo, *ACS Appl. Mater. Interfaces*, 2020, **12**, 32526–32535.

33 K. W. Nam, S. S. Park, R. dos Reis, V. P. Dravid, H. Kim, C. A. Mirkin and J. F. Stoddart, *Nat. Commun.*, 2019, **10**, 1–10.

34 J. Cao, D. Zhang, Y. Yue, X. Wang, T. Pakornchote, T. Bovornratanaraks, X. Zhang, Z. S. Wu and J. Qin, *Nano Energy*, 2021, **84**, 105876.

35 F. Tang, J. Gao, Q. Ruan, X. Wu, X. Wu, T. Zhang, Z. Liu, Y. Xiang, Z. He and X. Wu, *Electrochim. Acta*, 2020, **353**, 136570.

36 X. Wang, Z. Zhang, B. Xi, W. Chen, Y. Jia, J. Feng and S. Xiong, *ACS Nano*, 2021, **15**, 9244–9272.

37 J. Zhang, H. Feng, Q. Qin, G. Zhang, Y. Cui, Z. Chai and W. Zheng, *J. Mater. Chem. A*, 2016, **4**, 6357–6367.

38 C. Te Hsieh, S. M. Hsu, J. Y. Lin and H. Teng, *J. Phys. Chem. C*, 2011, **115**, 12367–12374.

39 Z. Liu, Y. Yang, S. Liang, B. Lu and J. Zhou, *Small Struct.*, 2021, **2**, 2100119.

40 X. Xie, H. Fu, Y. Fang, B. Lu, J. Zhou and S. Liang, *Adv. Energy Mater.*, 2021, **2102393**, 2102393.